

Article

Largest Magnetic Moments in the Half-Heusler Alloys XCrZ (X = Li, K, Rb, Cs; Z = S, Se, Te): A First-Principles Study

Xiaotian Wang ^{1,3} , Zhenxiang Cheng ³  and Guodong Liu ^{2,*}

¹ School of Physical Science and Technology, Southwest University, Chongqing 400715, China; wangxt45@126.com or xiaotianwang@swu.edu.cn

² College of Physics and Information Technology, Chongqing Normal University, Chongqing 401331, China

³ Institute for Superconducting & Electronic Materials (ISEM), University of Wollongong, Wollongong 2500, Australia; cheng@uow.edu.au

* Correspondence: gdliu1978@126.com

Received: 7 August 2017; Accepted: 12 September 2017; Published: 14 September 2017

Abstract: A recent theoretical work indicates that intermetallic materials LiMnZ (Z = N, P) with a half-Heusler structure exhibit half-metallic (HM) behaviors at their strained lattice constants, and the magnetic moments of these alloys are expected to reach as high as $5 \mu_B$ per formula unit. (Damewood et al. *Phys. Rev. B* **2015**, *91*, 064409). This work inspired us to find new Heusler-based half-metals with the largest magnetic moment. With the help of the first-principles calculation, we reveal that XCrZ (X = K, Rb, Cs; Z = S, Se, Te) alloys show a robust, half-metallic nature with a large magnetic moment of $5 \mu_B$ at their equilibrium and strained lattice constants in their most stable phases, while the excellent HM nature of LiCrZ (Z = S, Se, Te) alloys can be observed in one of their metastable phases. Moreover, the effects of uniform strain in LiCrZ (Z = S, Se, Te) alloys in type II arrangement have also been discussed.

Keywords: half-Heusler alloys; intermetallic materials; first-principles calculation

1. Introduction

In recent years, the fast development of spintronics [1] has caused more and more concern for researchers. Extensive applications (e.g., single spin electron sources [2] and spin injections [3]) have been envisaged [4]. One ideal choice for spintronics is the source of the spin-polarized charge carriers (SPCC). In this quest for materials, half-Heusler half-metallic alloys [5] are a noticeable family of intermetallic materials with 1:1:1 composition and have fully SPCC at the Fermi level.

The half-Heusler family has become one of the research hot-spots in intermetallic materials systems because the concept of half-metallic (HM) behaviors arose from the theoretical calculations by de Groot et al. for the well-known NiMnSb [6] in the 1980s. Then, quite a lot of half-Heusler alloys [7–15] had been predicted to be HM materials (HMMs). Recently, the electronic, magnetic, and stability properties were systematically investigated by first principles calculation in half-Heusler alloys of LiMnZ (Z = N, P, Si) [16]. Damewood et al. found that these LiMnZ (Z = N, P, Si) alloys show HM behaviors with large semiconducting-type band-gaps and magnetic moments ($>3 \mu_B$ per formula unit) at their strained lattice constants. To our best knowledge, based on the the Slater-Pauling (S-P) and generalized electron-filling rules [17–20], the largest magnetic moment of the half-Heusler-type alloy should be $5 \mu_B$ per formula unit. Due to the large semiconducting-type band-gaps and the large magnetic moments, LiMnZ (Z = N, P, Si) alloys may be good candidates for spintronic materials for devices operating at or above room temperature.

Based on the above information, it is necessary for us to further explore new HM half-Heusler alloys, XCrZ ($X = \text{Li, K, Rb, Cs}$; $Z = \text{S, Se, Te}$), with the largest magnetic moment ($5 \mu_B$ per formula unit) and large semiconducting-type band-gaps. In this work, first-principles calculations have been used to exhibit a theoretical study of the structural, electronic, magnetic, and HM properties of the XCrZ ($X = \text{Li, K, Rb, Cs}$; $Z = \text{S, Se, Te}$) half-Heusler alloys in three possible arrangements.

2. Computational Details

The electronic-structure and magnetism calculations were performed via CASTEP code on the basis of the pseudo-potential method with a plane-wave basis set [21,22]. The ultrasoft pseudo-potential [23] has been used to describe the interactions between the atomic core and the valence electrons. A most common generalized gradient approximation (GGA) [24] has been selected to describe the electron exchange-correlation. A plane-wave basis set cut-off of 450 eV and a mesh of $12 \times 12 \times 12$ k-points was used for Brillouin zone integrations. The convergence tolerance for the calculations was selected as a difference in total energy within 1×10^{-6} eV·atom⁻¹.

To determine the real-space bonding analysis, the electron localization function (ELF) was calculated using the CASTEP code. The ELF is a real-space indicator of the extent to which electrons are localized and display a strong Pauli repulsion, and therefore it can locate bonding and non-bonding electron pairs in the real-space of the crystal-structure [25,26].

3. Results and Discussion

Normally, half-Heusler alloys have a formula of XYZ. In this work, X is the Li, K, Rb, and Cs atoms, Y is the Cr atom, and Z is the main-group-element atoms S, Se, and Te. As shown in Figure 1, in the half-Heusler alloys XCrZ with the $C1_b$ structure, three possible arrangements have been taken into consideration: type I = [4c (0.25, 0.25, 0.25), 4d (0.75, 0.75, 0.75), 4a (0, 0, 0)], type II = [4a (0, 0, 0), 4d (0.75, 0.75, 0.75), 4c (0.25, 0.25, 0.25)] and type III = [4b (0.5, 0.5, 0.5), 4d (0.75, 0.75, 0.75), 4a (0, 0, 0)]. To obtain the equilibrium lattice structures of the XCrZ, the geometry optimization is firstly performed in their three possible arrangements. The achieved total energy-lattice constant curves for XCrZ are shown in Figure 2. Obviously, KCrS, RbCrS, CsCrS, KCrSe, and RbCrSe alloys have their lowest energies in type I instead of type II and III. For the CsCrSe, KCrTe, RbCrTe, and CsCrTe (LiCrS, LiCrSe, and LiCrTe) alloys, the structure of type III (type II), with the lowest energy, is the most stable among the three arrangements.

Table 1 shows for all XCrZ ($X = \text{Li, K, Rb, Cs}$; $Z = \text{S, Se, Te}$) the calculated total magnetic moments and the sizes of the semiconducting-type band-gaps. For the semiconducting-type band-gaps, the Fermi level (E_F) just falls within the gap in the spin-down band, indicating semiconductor properties. As can be observed in Table 1, the values of the total magnetic moment per formula unit (M_t) are $5 \mu_B$ for XCrZ ($X = \text{K, Rb, Cs}$; $Z = \text{S, Se, Te}$) in their most stable phases (arrangements). However, the calculated magnetic moments per formula unit for LiCrZ ($Z = \text{S, Se, Te}$) are not the integral Bohr magneton for the most stable phase. As is known, for the Heusler-type HMMs, their calculated M_t is usually an integer value [27–30]. The non-integer values of M_t for LiCrZ ($Z = \text{S, Se, Te}$) in type II indicate that they are not HMMs in the most stable phase. Also, as shown in Table 1, all XCrZ alloys have very large semiconducting-type band-gaps (>2 eV) in their most stable phase, except for LiCrZ ($Z = \text{S, Se, Te}$). It means that they may maintain their magnetic and HM behaviors at room temperature.

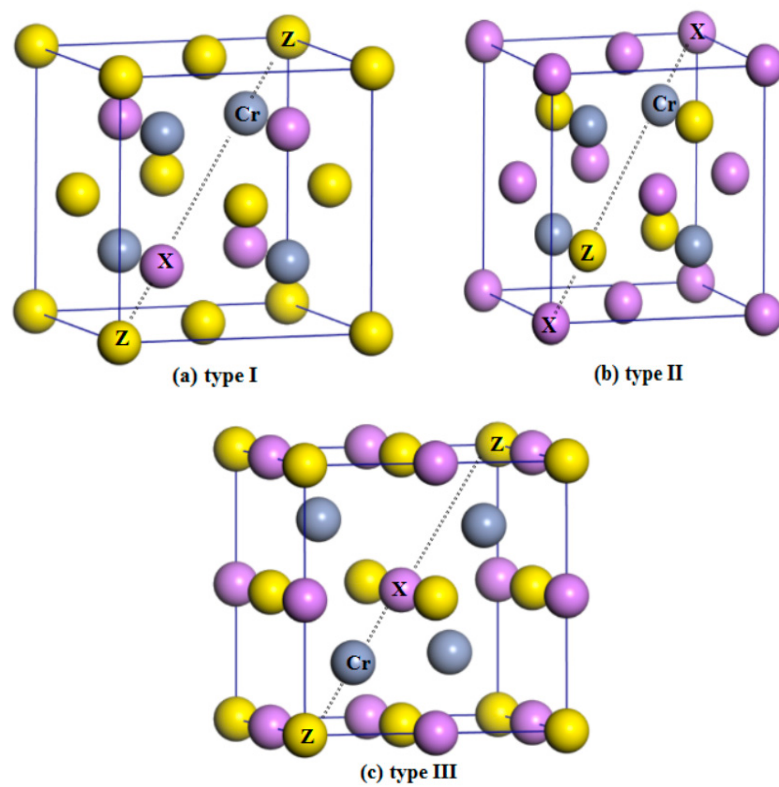


Figure 1. Crystal structures of the three arrangements within the half-Heusler alloys XCrZ (X = Li, K, Rb, Cs; Z = S, Se, Te) noted as type I (a); type II (b) and type III (c).

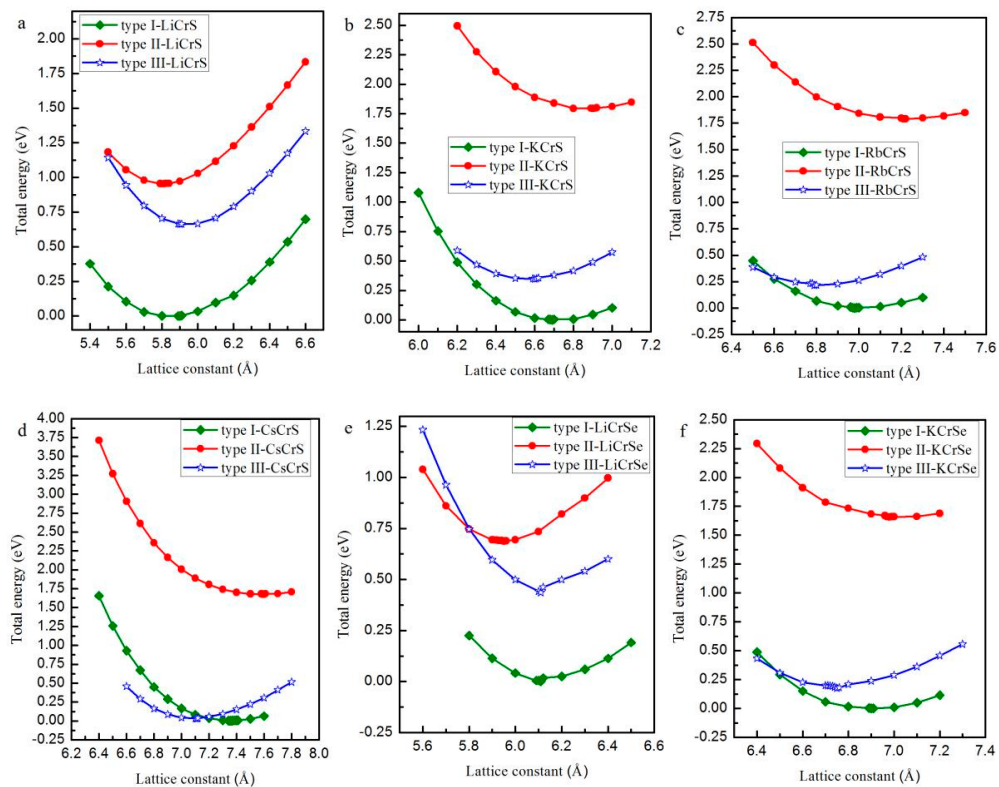


Figure 2. Cont.

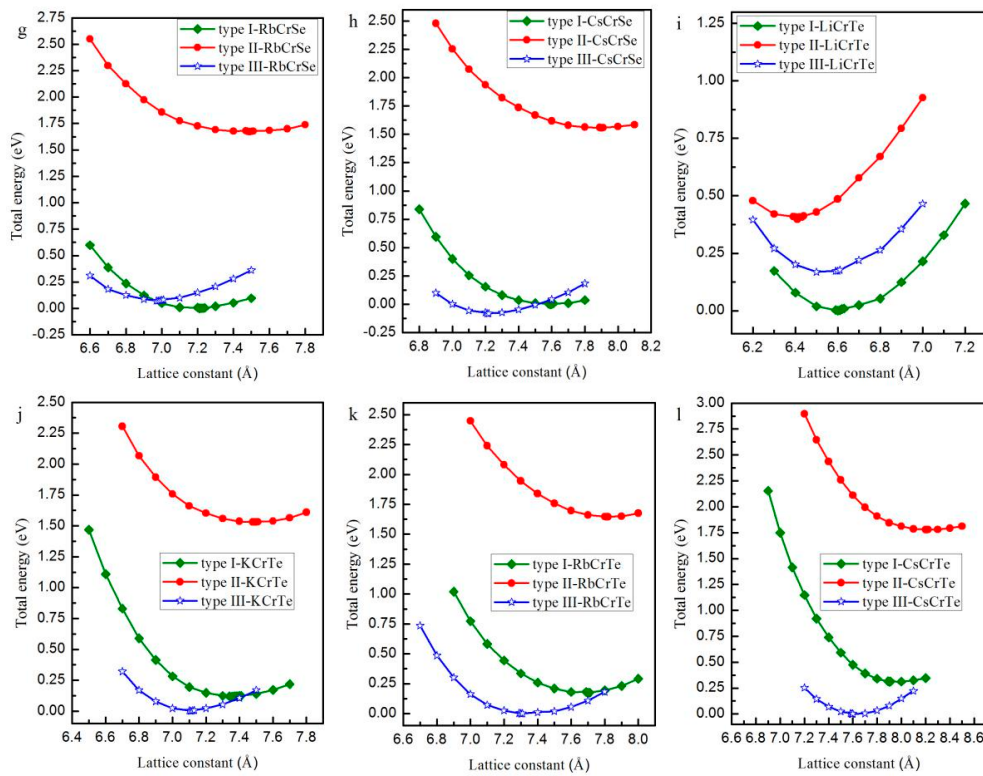


Figure 2. The total energy as a function of the lattice constant in the three atomic arrangements type I, type II, and type III for half-Heusler alloys LiCrS (a); KCrS (b); RbCrS (c); CsCrS (d); LiCrSe (e); KCrSe (f); RbCrSe (g); CsCrSe (h); LiCrTe (i); KCrTe (j); RbCrTe (k) and CsCrTe (l), respectively.

Table 1. Optimized lattice constants (a), calculated total and the atomic magnetic moments (M_t) per formula unit, and sizes of the semiconducting-type band-gap (Gap) at different crystal structures for $XCrZ$ ($X = \text{Li, K, Rb, Cs}$; $Z = \text{S, Se, Te}$). Yes (or no) indicates that this alloy is (or is not) a half metal.

Alloy	Type	a (Å)	M_{tot} (μ_B)	M_X	M_{Cr}	M_Z	Gap (eV)	HM Behavior
LiCrS	Type I	5.89	4.82	−0.08	5.04	−0.14	-	No
	Type II	5.82	5.00	−0.08	5.22	−0.12	3.62	Yes
	Type III	5.90	4.97	−0.02	5.18	−0.20	-	No
LiCrSe	Type I	6.19	4.92	−0.08	5.16	−0.16	-	No
	Type II	6.00	5.00	−0.04	5.36	−0.32	3.15	Yes
	Type III	6.11	4.97	0.04	5.30	−0.36	-	No
LiCrTe	Type I	6.60	4.95	−0.02	5.30	−0.32	-	No
	Type II	6.37	5.00	−0.02	5.42	−0.40	2.10	Yes
	Type III	6.60	4.94	0.02	5.40	−0.48	-	No
KCrS	Type I	6.71	5.00	−0.12	5.34	−0.22	3.15	Yes
	Type II	6.90	5.00	−0.32	5.54	−0.24	2.14	Yes
	Type III	6.60	5.00	−0.24	5.40	−0.18	3.41	Yes
KCrSe	Type I	6.91	5.00	−0.26	5.38	−0.12	2.85	Yes
	Type II	6.98	5.00	−0.12	5.58	−0.46	2.09	Yes
	Type III	6.75	5.00	−0.14	5.46	−0.34	3.07	Yes
KCrTe	Type I	7.35	5.00	−0.06	5.46	−0.42	2.87	Yes
	Type II	7.41	5.00	−0.08	5.66	−0.58	1.87	Yes
	Type III	7.11	5.00	−0.10	5.54	−0.46	2.92	Yes
RbCrS	Type I	7.01	5.00	−0.14	5.38	−0.24	2.65	Yes
	Type II	7.21	5.00	−0.30	5.56	−0.26	1.69	Yes
	Type III	6.79	5.00	−0.24	5.40	−0.18	3.19	Yes

Table 1. Cont.

Alloy	Type	a (Å)	M_{tot} (μ_B)	M_X	M_{Cr}	M_Z	Gap (eV)	HM Behavior
RbCrSe	Type I	7.21	5.00	−0.12	5.42	−0.30	2.33	Yes
	Type II	7.49	5.00	−0.08	5.64	−0.56	1.49	Yes
	Type III	6.98	5.00	−0.16	5.46	−0.30	2.72	Yes
RbCrTe	Type I	7.63	5.00	−0.04	5.50	−0.46	2.40	Yes
	Type II	7.81	5.00	−0.06	5.68	−0.62	1.54	Yes
	Type III	7.30	5.00	−0.12	5.54	−0.42	2.71	Yes
CsCrS	Type I	7.35	5.00	−0.14	5.42	−0.28	2.09	Yes
	Type II	7.59	5.00	−0.26	5.58	−0.30	1.41	Yes
	Type III	7.11	5.00	−0.22	5.40	−0.18	2.83	Yes
CsCrSe	Type I	7.54	5.00	−0.02	5.48	−0.46	2.01	Yes
	Type II	7.90	5.00	−0.04	5.68	−0.64	1.31	Yes
	Type III	7.21	5.00	−0.14	5.42	−0.28	2.61	Yes
CsCrTe	Type I	7.98	5.00	−0.02	5.52	−0.50	2.09	Yes
	Type II	8.21	5.00	−0.02	5.72	−0.70	1.31	Yes
	Type III	7.59	5.00	−0.12	5.54	−0.42	2.29	Yes

To further confirm the possible half-metallicity of $XCrZ$ ($X = K, Rb, Cs$; $Z = S, Se, Te$), we show in Figure 3 the calculated total and atom-projected DOS for $KCrS$, $RbCrS$, $CsCrS$, $KCrSe$, and $RbCrSe$ in the type I arrangement and $CsCrSe$, $KCrTe$, $RbCrTe$, and $CsCrTe$ in the type III arrangement, respectively. Obviously, it can be found that all these mentioned alloys show half-metallic behaviors: in the majority spin (spin-up) channel, the energy bands exhibit a metallic overlap with the E_F , whereas in the minority spin (spin-down) direction, an energy gap is opened and the E_F locates within the gap.

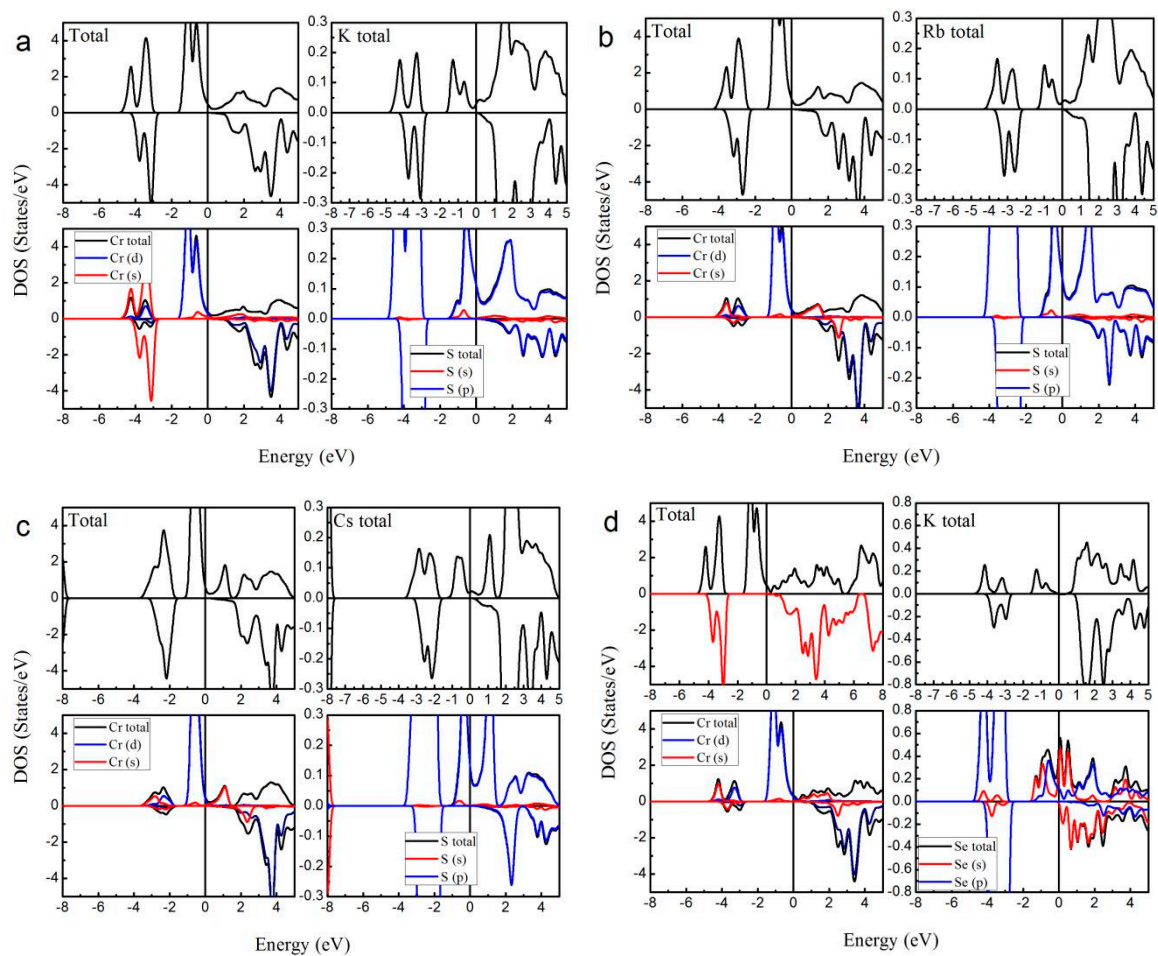


Figure 3. Cont.

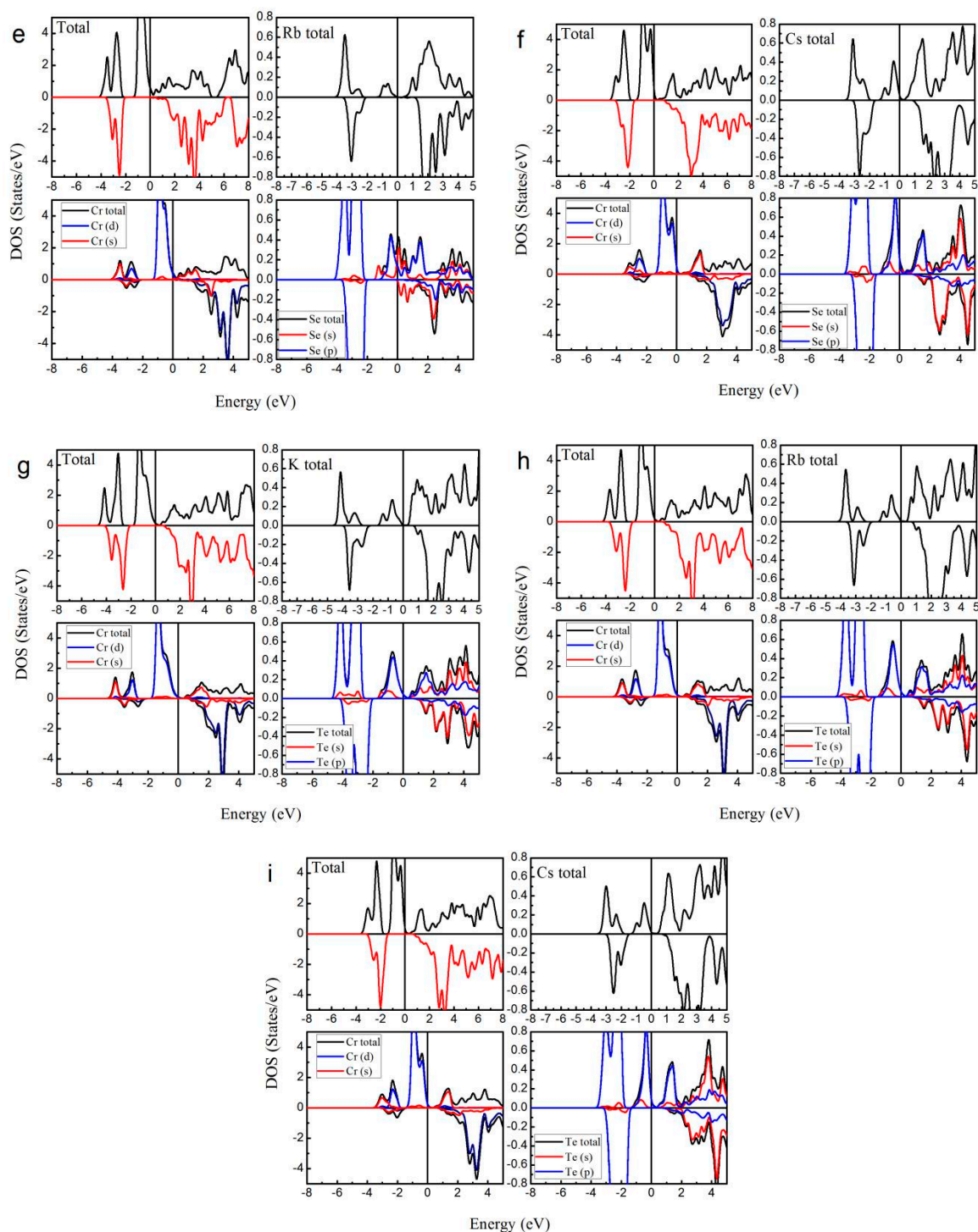


Figure 3. Calculated total and atom-projected density of states (DOS) for (a) type I KCrS; (b) type I RbCrS; (c) type I CsCrS; (d) type I KCrSe; (e) type I RbCrSe; (f) type III CsCrSe; (g) type III KCrTe; (h) type III RbCrTe; and (i) type III CsCrTe. (The Fermi level E_F was set as $X = 0$).

It is common sense that the DOS can be widely used to discuss the bonding/anti-bonding states and the gap formation, and we should also point out that a similar analytical approach used in this work can be observed in [31,32].

Figure 3 shows the total density of states (TDOS) and the partial density of states (PDOS) of XCrZ ($X = \text{K, Rb, Cs}$; $Z = \text{S, Se, Te}$) in the most stable phase. Obviously, in both spin channels, the main

contributions to the TDOS around the Fermi level arose from the 3d states of the Cr atom. The X and Z atoms have a rather lower PDOS than the Cr atom.

As shown in Figure 3, in the spin-up channel the main peaks of the Cr and Z atoms occurred in the range from -2 eV to 0 eV, and -4 eV to -2 eV, respectively. Meanwhile, between the -4 eV and -2 eV states, similar-shaped, hybridized peaks can also be found in the Cr atoms. In the spin-down channel, in the same energy range (-4 eV \sim -2 eV), for the Cr and Z atoms, such hybridized peaks appeared at the same time. Therefore, the hybridization between the Cr and Z atoms that formed strong bonding states range from -4 eV to -2 eV. Above the E_F , in the spin-down channel, the anti-bonding can be found at around 3 eV, and in the spin-up channel, no opposite energy states are observed. Moreover, similar to the LiMnZ alloys [16], the bonding-antibonding states led to the formation of a semiconducting-type band-gap in the spin-down channel.

For the type I and type III arrangements, the semiconducting-type band-gaps of the XCrZ ($X = \text{K, Rb, Cs}$; $Z = \text{S, Se, Te}$) alloys are very large. However, compared to the type I and type III arrangements, the type II arrangement does not form a large semiconducting-type band-gap (see Table 1) because the Cr and Z are second neighbors in a cubic environment.

In addition, as mentioned above, the calculated M_t , $5 \mu_B$ for XCrZ ($X = \text{K, Rb, Cs}$; $Z = \text{S, Se, Te}$) follows the modified S-P rule recently presented by Damewood et al. [16],

$$M_t = (Z_t - 8) \cdot \mu_B, \quad (1)$$

here Z_t is the number of total of valence electrons in XCrZ ($X = \text{K, Rb, Cs}$; $Z = \text{S, Se, Te}$), respectively.

Furthermore, the total M_t for the XCrZ ($X = \text{K, Rb, Cs}$; $Z = \text{S, Se, Te}$) alloys at their strained lattice constants with the most stable phase has been calculated, and the results are shown in Figure 4. Obviously, for all these mentioned alloys, the total M_t of $5.00 \mu_B/\text{f.u}$ remained constant within an expansion and contraction of less than $0.01 \mu_B$ over a large range of lattice constant values. That is to say, the half-metallic behavior of these alloys is quite robust. When the lattice constants are compressed to the critical value 5.99 \AA for KCrS, 5.84 \AA for RbCrS, 5.92 \AA for CsCrS, 6.16 \AA for KCrSe, 6.01 \AA for RbCrSe, 6.60 \AA for CsCrSe, 6.65 \AA for KCrTe, 6.69 \AA for RbCrTe, and 6.92 \AA for CsCrTe, respectively, the semiconducting-type band-gap in the spin-down channel closed and thus the integer value of the total magnetic moments disappeared.

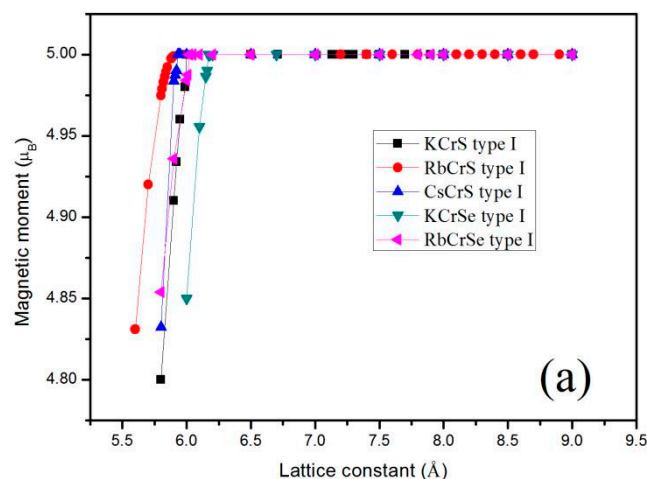


Figure 4. Cont.

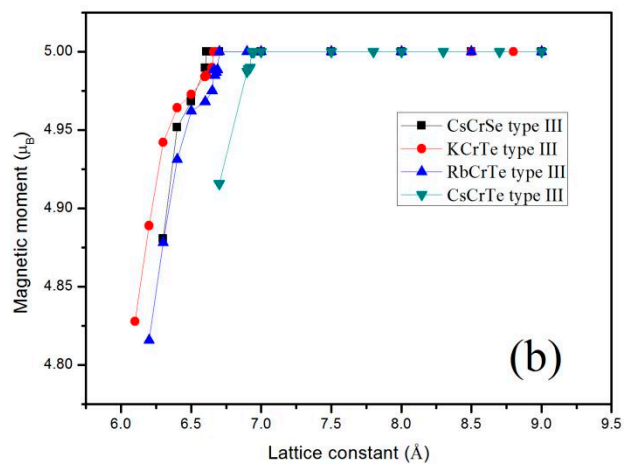


Figure 4. Calculated total magnetic moments as functions of the lattice constant for KCrS, RbCrS, CsCrS, KCrSe, RbCrSe (a) and CsCrSe, KCrTe, RbCrTe, CsCrTe (b), respectively, with their most stable phase.

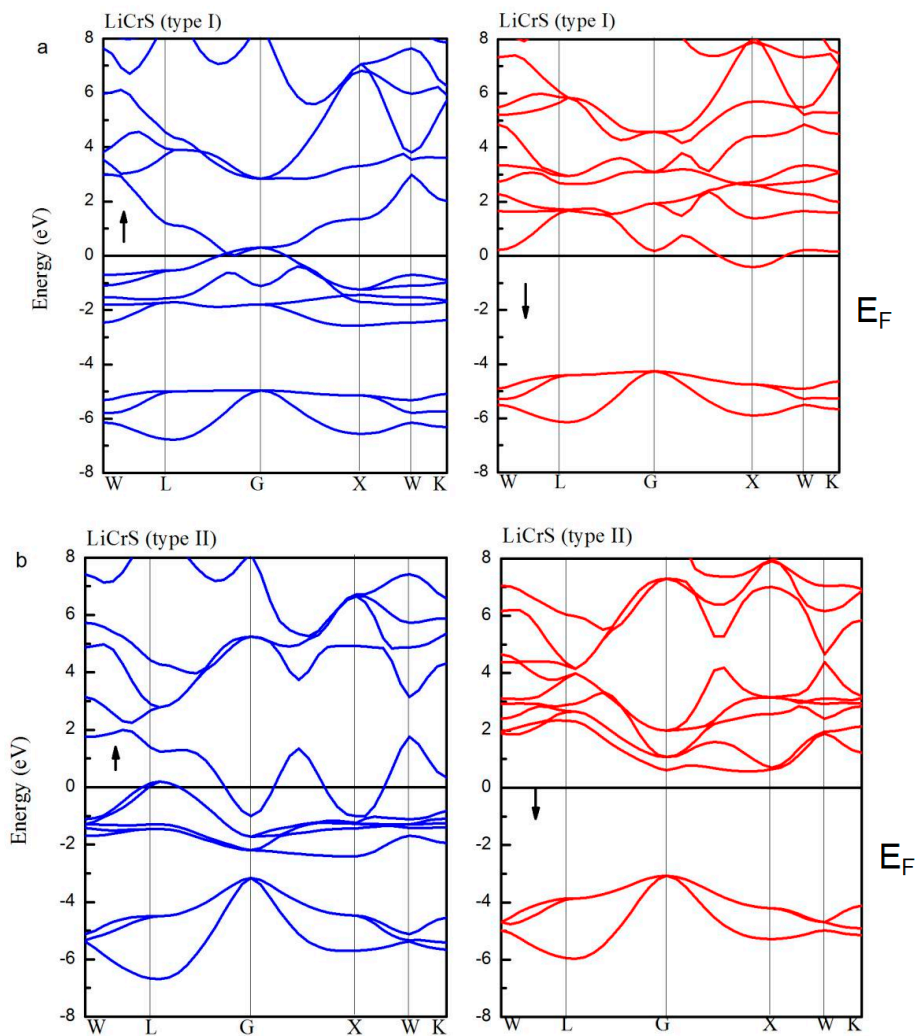


Figure 5. Cont.

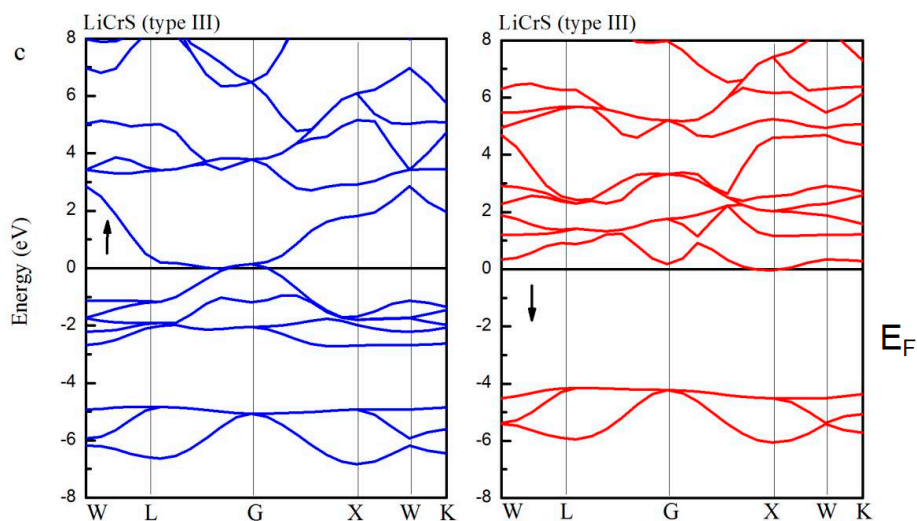


Figure 5. The spin-up (blue lines) and spin-down (red lines) band structures for LiCrS alloy in the three atomic (type I (a); type II (b); and type III (c)) arrangements. (The Fermi level E_F was set as $Y = 0$).

Previous studies have shown that ternary alloys, including the Li atom, are good candidates in optoelectronic and spintronic applications [33,34]. Although the LiCrZ alloys presented in the current work are not HMMs (see Table 1) in the most stable arrangement (type I), the other arrangements (type II and III) should also be reported here to check the electronic, magnetic, and half-metallic properties. We hope to search for a metastable (type II or III) of the LiCrZ ($Z = S, Se, Te$) alloys exhibiting HM behavior with the largest magnetic moment ($5 \mu_B$) and a large semiconducting-type band-gap (>2 eV).

Figure 5 shows the spin-up (blue lines) and spin-down (red lines) band structures for the LiCrS alloy in the three atomic (type I, type II, and type III) arrangements. Definitely, in the type I and III arrangements, in both the spin channels, the E_F overlaps with the energy bands. However, the LiCrS in the type II arrangement exhibits a half-metallic nature, namely, the majority spin electrons show metallic behaviors and the minority spin electrons exhibit semiconducting properties. Similar behaviors were also discovered in the LiCrSe and LiCrTe alloys. The indirect semiconducting-type band-gaps of the LiCrZ ($Z = S, Se, Te$) alloys in the type II arrangement are 3.62 eV, 3.15 eV, and 2.10 eV, respectively, and are also listed in Table 1.

As a representative of all the LiCrZ alloys, in Figure 6, we display the calculated total and atom-projected DOS, and the ELF graphs of the LiCrS alloy in the three atomic arrangements (type I, type II, and type III). For the type II arrangement, in the minority spin channel, the antibonding peak is shifted high above E_F due to the exchange splitting [18], whereas for the case of the type I and III arrangements, the minority DOS, together with the energy gap, moves to low energy. Moreover, we also perform the ELF maps project on the (1 1 0) plane of the LiCrS in types I, II, and III, respectively. The high- and low- ELF values in the graphs of ELF correspond to areas of localized electrons and the area around the maxima, respectively [35]. As shown in Figure 6a,c, for the type I and type III arrangements, the regions of the highest ELF value are all around the main-group S atom along the S-Cr bound axes, indicating their sharing behavior and the occurrence of the covalent bond. We should note that, for the type I and III arrangements, the S and Cr atoms are nearest neighbors and show strong S-Cr covalent-hybridization. However, for the type II arrangement, the S and Cr atoms sit by the second neighbor sites and show nearly no S-Cr covalent-hybridization.

In the half-Heusler alloys LiCrZ ($Z = S, Se, Te$), through the DOS and the ELF maps, we can summarize the electronic structure into the following two features: (i) under the strong S-Cr covalent-hybridization, LiCrZ ($Z = S, Se, Te$) alloys with both type I and type III arrangements show typically metallic band structure; (ii) under less S-Cr covalent-hybridization, LiCrZ with type II

arrangement takes on excellent half-metallic band behavior with largest magnetic moment $5 \mu_B$ at the equilibrium lattice constant.

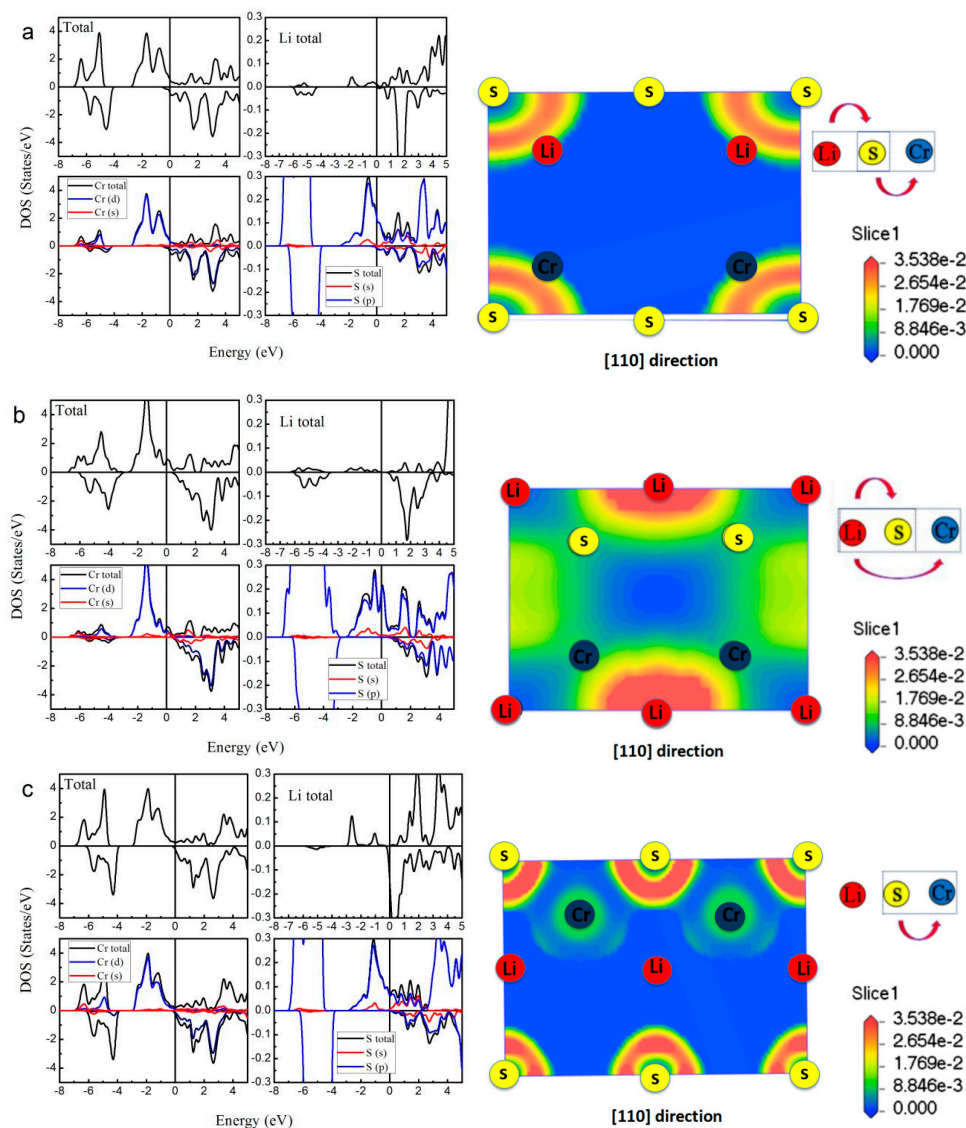


Figure 6. Calculated total and atom-projected DOS, and the electron localization function (ELF) graphs of the LiCrS alloy in the three atomic arrangements: type I (a); type II (b); and type III (c). (The Fermi level E_F was set as $X = 0$).

In the spintronic devices, the Heusler type HM multilayers or thin films are often touched by researchers; however, the actual and ideal lattice constants are usually inconsistent. The change of the lattice constants will lead to significant changes of the electronic, magnetic, and HM properties of the equilibrium state. Hence, we need to examine the HM stability for the LiCrZ ($Z = S, Se, Te$) in the type II arrangement at the strained lattice constants. The band-structure calculations at the strained lattice constants were performed for the LiCrZ ($Z = S, Se, Te$) alloys in the type II arrangement. In this discussion, the values of CBM and VBM for the LiCrZ ($Z = S, Se, Te$) alloys in the minority spin channel have been recorded to show the HM behavior for clarity, as plotted in Figure 7. Obviously, the HM states are kept for the lattice constants of 5.57–6.50 Å for LiCrS, 5.71–6.36 Å for LiCrSe, and 6.15–7.94 Å for LiCrTe, respectively. That is, these three alloys can maintain their half-metallicity when their

lattice constants are changed by -4.2% to 11.68% , -4.83% to 6% , and -3.45% to 24.64% relative to the equilibrium lattice constants.

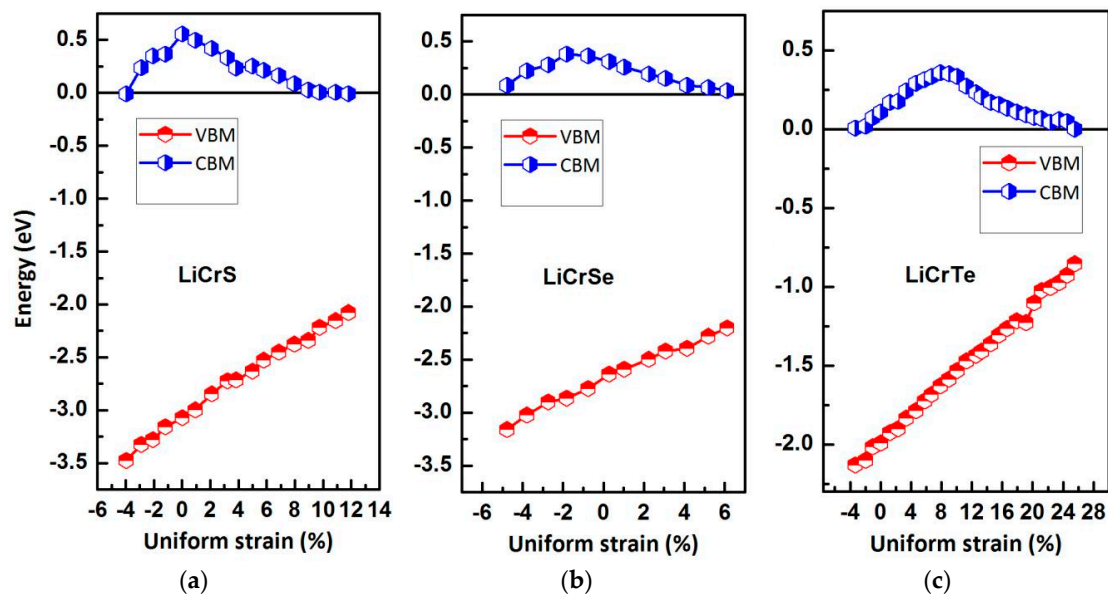


Figure 7. Calculated valence band maximum (VBM) and conduction band minimum (CBM) as a function of the lattice constants for the LiCrS (a), LiCrSe (b) and LiCrTe (c) alloys in the type II arrangement. The black circle and the red circle represent the VBM and CBM, respectively. (The Fermi level E_F was set as $Y = 0$).

In Figure 8, we show the relationship between the M_t and the lattice constant of type II LiCrZ ($Z = S, Se, Te$). Obviously, the total M_t is always a fixed integer value $5 \mu_B$ in the whole variational range. The atomic M_t of Cr and Z are sensitive to lattice distortion. The M_t of the Cr atom increases with increasing lattice constants, whereas for the Z ($Z = S, Se, Te$) atom they continuously decrease.

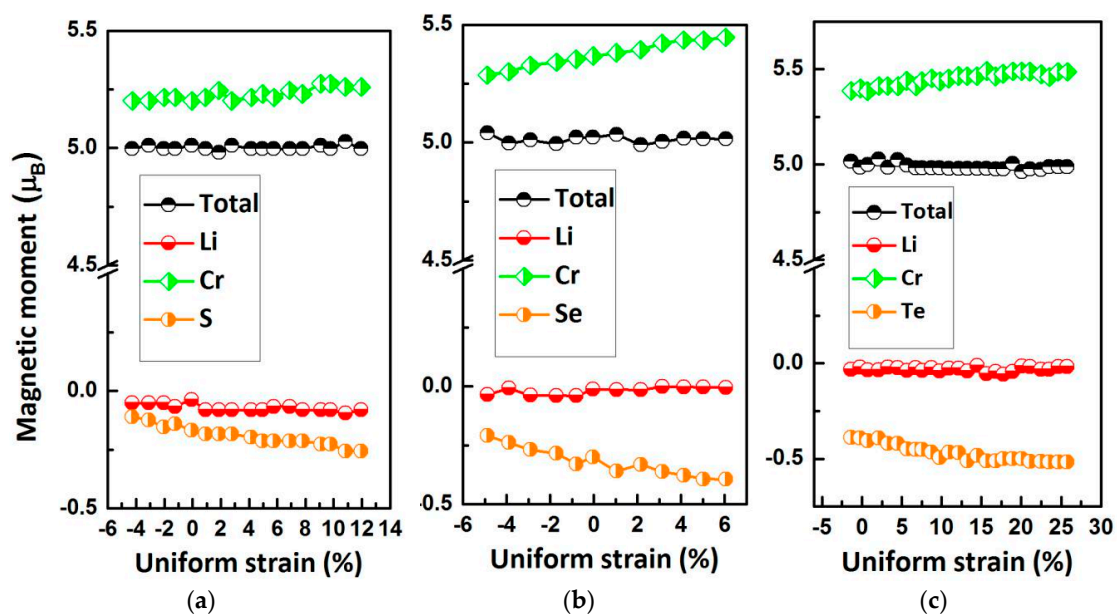


Figure 8. Total and atomic magnetic moments as functions of the lattice constants for the LiCrS (a), LiCrSe (b) and LiCrTe (c) alloys in type II arrangement.

Our work suggests that the XCrZ (X = Li, K, Rb, Cs; Z = S, Se, Te) half-Heusler alloys are useful in spintronic applications. For the half-Heusler type XCrZ (X = K, Rb, Cs; Z = S, Se, Te) alloys, their formation energies have been calculated based on the following formula:

$$E_{formation} = E_{XCrZ}^{total} - (E_X^{bulk} + E_{Cr}^{bulk} + E_Z^{bulk}), \quad (2)$$

where E_{XCrZ}^{total} is the total energy of XCrZ per formula unit, and E_X^{bulk} , E_{Cr}^{bulk} , and E_Z^{bulk} are the total energies per atom of each element in the bulk for the X, Cr, and Zr, respectively. The results have been shown in Figure 9; the negative formation energies indicate that these alloys are expected to be stable. Therefore, they have the large change to be synthesized by normal equilibrium methods (e.g., arc-melting). However, for LiCrZ (Z = S, Se, Te), some non-equilibrium methods (e.g., rapid quenching) can be selected to prepare these meta-stable compounds [36].

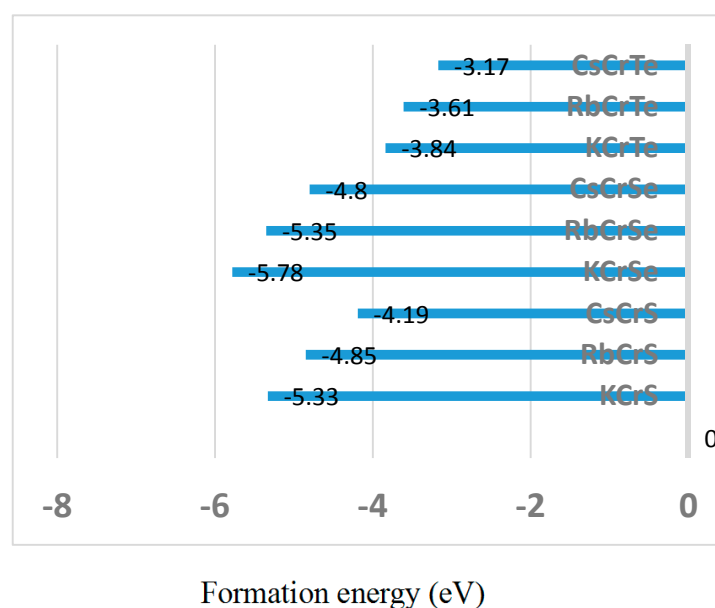


Figure 9. Calculated formation energies (eV) for the XCrZ (X = K, Rb, Cs; Z = S, Se, Te) alloys with the most stable phase.

4. Conclusions

A first principles calculation was used to predict a series of new half-Heusler-based, half-metallic materials XCrZ (X = Li, K, Rb, Cs; Z = S, Se, Te) with the largest magnetic moment ($5 \mu_B$) and large semiconducting-type band-gaps (>2 eV). In detail, for XCrZ (X = K, Rb, Cs; Z = S, Se, Te), the HM nature of these alloys appeared at their equilibrium and strained lattice constants and in their most stable phases. However, for the LiCrZ alloys, the HM behaviors of these alloys did not appear in the most stable phase but in one of the metastable phases. The half-metallicity of the XCrZ alloys is robust against uniform strain, which makes these alloys very stable with respect to the spin polarization properties.

Acknowledgments: Z.X. Cheng thanks the Australian Research Council for support. Funding for this research was provided by: Scientific Research Project for High Level Talent in Colleges and Universities of Hebei Province (No. GCC 2014042), Natural Science Foundation of Hebei Province (No. E2016202383), Chongqing City Funds for Distinguished Young Scientists (No. cstc2014jcyj50003), and the Program for Leading Talents in Science and Technology Innovation of Chongqing City (No. CSTCKJXCLJRC19).

Author Contributions: Zhenxiang Cheng and Guodong Liu designed the project, Xiaotian Wang performed the calculations and prepared the manuscript, and all authors analyzed the data and discussed the results.

Conflicts of Interest: The authors declare no conflict of interest.

References

1. Žutić, I.; Fabian, J.; Sarma, S.D. Spintronics: Fundamentals and applications. *Rev. Mod. Phys.* **2004**, *76*, 323–410. [[CrossRef](#)]
2. Park, J.H.; Vescovo, E.; Kim, H.; Kwon, C. Direct evidence for a half-metallic ferromagnet. *Nature* **1998**, *392*, 794–796. [[CrossRef](#)]
3. Wang, Y.Y.; Wu, M.W. Schottky-barrier-induced spin relaxation in spin injection. *Phys. Rev. B* **2005**, *72*, 153301. [[CrossRef](#)]
4. Hashemifar, S.J.; Kratzer, P.; Scheffler, M. Preserving the half-metallicity at the Heusler alloy Co_2MnSi (001) surface: A density functional theory study. *Phys. Rev. Lett.* **2005**, *94*, 096402. [[CrossRef](#)] [[PubMed](#)]
5. Lin, H.; Wray, L.A.; Xia, Y.; Xu, S.; Jia, S.; Cava, R.J.; Hasan, M.Z. Half-Heusler ternary compounds as new multifunctional experimental platforms for topological quantum phenomena. *Nat. Mater.* **2010**, *9*, 546–549. [[CrossRef](#)] [[PubMed](#)]
6. De Groot, R.A.; Mueller, F.M.; Van Engen, P.G.; Buschow, K.H.J. New class of materials: Half-metallic ferromagnets. *Phys. Rev. Lett.* **1983**, *50*, 2024. [[CrossRef](#)]
7. Khalaf Alzyadi, J.M.; Jolan, M.H.; Yao, K.L. Surface half-metallicity of half-Heusler compound FeCrSe and interface half-metallicity of FeCrSe/Gap. *J. Magn. Magn. Mater.* **2016**, *403*, 8–13. [[CrossRef](#)]
8. Lakdja, A.; Rozale, H.; Chahed, A.; Benhelal, O. Ferromagnetism in the half-Heusler XCsBa compounds from first-principles calculations (X = C, Si, and Ge). *J. Alloys Compd.* **2013**, *564*, 8–12. [[CrossRef](#)]
9. Lakdja, A.; Rozale, H.; Sayede, A.; Chahed, A. Origin of ferromagnetism in the half-Heusler XRbCs compounds (X = N, P and As). *J. Magn. Magn. Mater.* **2014**, *354*, 235–238. [[CrossRef](#)]
10. Sedeeq, K.; Hantour, H.; Makram, N.; Said, S.A. Observation of strong ferromagnetism in the half-Heusler compound cotisb system. *J. Magn. Magn. Mater.* **2016**, *407*, 218–223. [[CrossRef](#)]
11. Rozale, H.; Amar, A.; Lakdja, A.; Moukadem, A.; Chahed, A. Half-metallicity in the half-Heusler RbSrC, RbSrSi and RbSrGe compounds. *J. Magn. Magn. Mater.* **2013**, *336*, 83–87. [[CrossRef](#)]
12. Białek, B.; Lee, J.I.; Kim, M. The surface electronic properties of newly designed half-metallic ferromagnets: GeKCa and SnKCa. *Comput. Mater. Sci.* **2014**, *81*, 510–516. [[CrossRef](#)]
13. Umamaheswari, R.; Vijayalakshmi, D.; Kalpana, G. First-principles calculation of structural, electronic and magnetic properties of half-Heusler LiCaC and NaCaC compounds. *Phys. B Condens. Matter* **2014**, *448*, 256–259. [[CrossRef](#)]
14. Chen, J.; Gao, G.Y.; Yao, K.L.; Song, M.H. Half-metallic ferromagnetism in the half-Heusler compounds GeKCa and SnKCa from first-principles calculations. *J. Alloys Compd.* **2011**, *509*, 10172–10178. [[CrossRef](#)]
15. Ahmad, M.; Murtaza, G.; Khenata, R.; Omran, S.B.; Bouhemadou, A. Structural, elastic, electronic, magnetic and optical properties of RbSrX (X = C, Si, Ge) half-Heusler compounds. *J. Magn. Magn. Mater.* **2015**, *377*, 204–210. [[CrossRef](#)]
16. Damewood, L.; Busemeyer, B.; Shaughnessy, M.; Fong, C.Y.; Yang, L.H.; Felser, C. Stabilizing and increasing the magnetic moment of half-metals: The role of Li in half-Heusler LiMnZ (Z = N, P, Si). *Phys. Rev. B* **2015**, *91*, 064409. [[CrossRef](#)]
17. Zhang, X.M.; Xu, G.Z.; Du, Y.; Liu, E.K.; Liu, Z.Y.; Liu, G.D.; Wu, G.H. Phase stability, magnetism and generalized electron-filling rule of vanadium-based inverse Heusler compounds. *Europhys. Lett.* **2013**, *104*, 27012. [[CrossRef](#)]
18. Fecher, G.H.; Kandpal, H.C.; Wurmehl, S.; Felser, C.; Schönhense, G. Slater-pauling rule and Curie temperature of Co_2 -based Heusler compounds. *J. Appl. Phys.* **2006**, *99*, 08J106. [[CrossRef](#)]
19. Zhang, L.; Wang, X.; Cheng, Z. Electronic, magnetic, mechanical, half-metallic and highly dispersive zero-gap half-metallic properties of rare-earth-element-based quaternary Heusler compounds. *J. Alloys Compd.* **2017**, *718*, 63–74. [[CrossRef](#)]
20. Gao, G.Y.; Hu, L.; Yao, K.L.; Luo, B.; Liu, N. Large half-metallic gaps in the quaternary Heusler alloys CoFeCrZ (Z = Al, Si, Ga, Ge): A first-principles study. *J. Alloys Compd.* **2013**, *551*, 539–543. [[CrossRef](#)]
21. Payne, M.C.; Teter, M.P.; Allan, D.C.; Arias, T.A.; Joannopoulos, J.D. Iterative minimization techniques for ab initio total-energy calculations: Molecular dynamics and conjugate gradients. *Rev. Mod. Phys.* **1992**, *64*, 1045. [[CrossRef](#)]

22. Segall, M.D.; Lindan, P.J.; Probert, M.A.; Pickard, C.J.; Hasnip, P.J.; Clark, S.J.; Payne, M.C. First-principles simulation: Ideas, illustrations and the CASTEP code. *J. Phys. Condens. Matter* **2002**, *14*, 2717–2744. [[CrossRef](#)]
23. Vanderbilt, D. Soft self-consistent pseudopotentials in a generalized eigenvalue formalism. *Phys. Rev. B* **1990**, *41*, 7892–7895. [[CrossRef](#)]
24. Perdew, J.P.; Burke, K.; Ernzerhof, M. Generalized gradient approximation made simple. *Phys. Rev. Lett.* **1996**, *77*, 3865–3868. [[CrossRef](#)] [[PubMed](#)]
25. Becke, A.D.; Edgecombe, K.E.A. Simple measure of electron localization in atomic and molecular systems. *J. Chem. Phys.* **1990**, *92*, 5397–5403. [[CrossRef](#)]
26. Silvi, B.; Savin, A. Classification of chemical bonds based on topological analysis of electron localization functions. *Nature* **1994**, *371*, 683–686. [[CrossRef](#)]
27. Wang, X.; Cheng, Z.; Wang, J.; Wang, L.; Yu, Z.; Fang, C.; Liu, G. Origin of the half-metallic band-gap in newly designed quaternary Heusler compounds $ZrVTiZ$ ($Z = Al, Ga$). *RSC Adv.* **2016**, *6*, 57041–57047. [[CrossRef](#)]
28. Birsan, A. Small interfacial distortions lead to significant changes of the half-metallic and magnetic properties in Heusler alloys: The case of the new $CoFeZrSi$ compound. *J. Alloys Compd.* **2017**, *710*, 393–398. [[CrossRef](#)]
29. Wei, X.P.; Zhang, Y.L.; Wang, T.; Sun, X.W.; Song, T.; Guo, P.; Deng, J.B. Stability, electronic and magnetic properties investigations on Zr_2YZ ($Y = Co, Cr, V$ and $Z = Al, Ga, In, Pb, Sn, Tl$) compounds. *Mater. Res. Bull.* **2017**, *86*, 139–145. [[CrossRef](#)]
30. Wang, X.T.; Cui, Y.T.; Liu, X.F.; Liu, G.D. Electronic structures and magnetism in the Li_2AgSb -type Heusler alloys, Zr_2CoZ ($Z = Al, Ga, In, Si, Ge, Sn, Pb, Sb$): A first-principles study. *J. Magn. Magn. Mater.* **2015**, *394*, 50–59. [[CrossRef](#)]
31. Zhang, Y.J.; Liu, Z.H.; Liu, G.D.; Ma, X.Q. Half-metallic fully compensated ferrimagnetism in $C1_b$ -type half heusler compounds $Mn_2Si_{1-x}Ge_x$. *J. Magn. Magn. Mater.* **2015**, *387*, 67–71. [[CrossRef](#)]
32. Zhang, Y.J.; Liu, Z.H.; Liu, E.K.; Liu, G.D.; Ma, Q.X.; Wu, G.H. Towards fully compensated ferrimagnetic spin gapless semiconductors for spintronic applications. *Europhys. Lett.* **2015**, *111*, 37009. [[CrossRef](#)]
33. Kieven, D.; Klenk, R.; Naghavi, S.; Felser, C.; Gruhn, T. I-II-V half-Heusler compounds for optoelectronics: Ab initio calculations. *Phys. Rev. B* **2010**, *81*, 075208. [[CrossRef](#)]
34. Jungwirth, T.; Novák, V.; Martí, X.; Cukr, M.; Máca, F.; Shick, A.B.; Zemek, J. Demonstration of molecular beam epitaxy and a semiconducting band structure for I-Mn-V compounds. *Phys. Rev. B* **2011**, *83*, 035321. [[CrossRef](#)]
35. Zhang, X.M.; Xu, G.Z.; Liu, E.K.; Liu, Z.Y.; Wang, W.H.; Wu, G.H. On the influence of tetrahedral covalent-hybridization on electronic band structure of topological insulators from first principles. *J. Appl. Phys.* **2015**, *117*, 045706. [[CrossRef](#)]
36. Luo, H.; Xin, Y.; Liu, B.; Meng, F.; Liu, H.; Liu, E.; Wu, G. Competition of L2 1 and XA structural ordering in Heusler alloys X_2CuAl ($X = Sc, Ti, V, Cr, Mn, Fe, Co, Ni$). *J. Alloys Compd.* **2016**, *665*, 180–185. [[CrossRef](#)]

